PHYSICS OF PLASMAS **15**, 012103 (2008)

Spectral gap of shear Alfvén waves in a periodic array of magnetic mirrors

Yang Zhang, W. W. Heidbrink, H. Boehmer, and R. McWilliams
Department of Physics and Astronomy, University of California, Irvine, California 92697, USA

Guangye Chen
Department of Aerospace Engineering and Engineering Mechanics, University of Texas, Austin, Texas 78712, USA

B. N. Breizman
Institute for Fusion Studies, University of Texas, Austin, Texas 78712, USA

S. Vincena, T. Carter, D. Leneman, W. Gekelman, P. Pribyl, and B. Brugman
Department of Physics and Astronomy, University of California, Los Angeles, California 90095, USA

(Received 17 August 2007; accepted 29 November 2007; published online 8 January 2008)

A multiple magnetic mirror array is formed at the Large Plasma Device (LAPD) [W. Gekelman, H. Pfister, Z. Lucky, J. Bamber, D. Leneman, and J. Maggs, Rev. Sci. Instrum. **62**, 2875 (1991)] to study axial periodicity-influenced Alfvén spectra. Shear Alfvén waves (SAW) are launched by antennas inserted in the LAPD plasma and diagnosed by B-dot probes at many axial locations. Alfvén wave spectral gaps and continua are formed similar to wave propagation in other periodic media due to the Bragg effect. The measured width of the propagation gap increases with the modulation amplitude as predicted by the solutions to Mathieu's equation. A two-dimensional finite-difference code modeling SAW in a mirror array configuration shows similar spectral features. Machine end-reflection conditions and damping mechanisms including electron-ion Coulomb collision and electron Landau damping are important for simulation. © *2008 American Institute of Physics*. [DOI: 10.1063/1.2827518]

I. INTRODUCTION

Waves propagating in periodic media have spectra with allowed bands separated by forbidden gaps. This phenomenon was first discussed in 1887 (Ref. 1) by Strutt (Lord Rayleigh) who recognized that it is characterized by the Hill and Mathieu differential equations. One naturally existing periodic system is a metallic crystal lattice, where the valence electron wave function couples with the one propagating in the opposite direction when the Bragg condition[2] is satisfied as

$$k = k_n \equiv n\pi/L, \tag{1}$$

where k is the wave number, L is the distance between two adjacent ions in the lattice, and n is an integer. Two standing wave solutions are formed corresponding to two distinct energy states with a prohibited energy gap in between. For electromagnetic waves, similar propagation frequency gaps occur in many periodic systems, e.g., optical fiber Bragg gratings, distributed feedback lasers (DFL),[3,4] and waveguide Bragg reflectors.[5,6] When the perfect translational symmetry is disrupted by a defect, e.g., donor/acceptor atoms in a semiconductor or holes in a photonic crystal,[7,8] eigenmodes can exist with frequencies inside the gap.

The propagation of TE and TM waves are treated analytically in a plasma with a stratified density profile in 1968,[9] where the spectral gap and continuum structures are found for both waves. Similar phenomena occur for Alfvén waves in magnetically confined plasmas.[10] The Alfvén speed v_A depends on the magnetic field B_0 and plasma mass density as $v_A = B_0/\sqrt{\mu_0 n_i m_i}$, so periodic variations in either the magnetic field or the mass density introduce periodic variations in the index of refraction. Gaps in the shear Alfvén wave spectrum are associated with periodic variations in B_0 caused by toroidicity,[11] elongation,[12] or triangularity[13] of flux surfaces, and many other geometrical effects.[14] The bands of propagation between these spectral gaps are called the Alfvén continuum. Excitations in the continuum usually damp rapidly due to phase mixing.

Spectral gaps are important in fusion energy research because weakly damped global eigenmodes that are readily destabilized by energetic ions often reside in these gaps. Fast ions expelled by these instabilities have damaged vessel components in some experiments,[15,16] so it is important for the practical realization of fusion energy to understand these Alfvén gap instabilities. The toroidicity-induced Alfvén eigenmode[17] (TAE) is the most extensively studied of these gap modes but numerous other modes that are excited by energetic particles also exist.[18] The phenomena of spectral gaps, gap modes, and fast-particle excitation are generic.

The goal of this work is to study shear Alfvén wave (SAW) propagation and forbidden gap formation in a periodic magnetic mirror array. The experiments are performed in the Large Plasma Device (LAPD). Although the number of mirror cells is limited, the LAPD is capable of generating a magnetic mirror array resembling the multimirror magnetic confinement fusion devices[19,20] in Novosibirsk, Russia. An advantage of the low-temperature plasma in the LAPD is its accessibility to a variety of probes. Alfvén wave propagation and interference can be studied with spatial resolution of ~1–10 mm. To further investigate the Alfvén spectral gaps and continua, a cold-plasma wave code[21] is adapted to launch Alfvén waves in a virtual LAPD with the number of mirror cells ranging from a few to infinite. Measured plasma parameters are used in the code to simulate wave spectra which are compared with experimental observations.

This paper presents the first experimental observation of an Alfvén spectral gap in a periodic magnetic mirror array. The remainder of this paper is organized as follows: In Sec. II, the previous studies of Alfvén waves in the LAPD are reviewed first and analytical results from Mathieu's equation are introduced for the SAW spectral gap in an infinite magnetic mirror array. The experimental setup, including the mirror array configuration and plasma and wave diagnostics, are introduced in Sec. III. Major results including the spectral gap dependence on mirror array parameters are presented in Sec. IV. Numerical simulation of the mirror-induced spectral features is presented in Sec. V. The correlation of this research to the Alfvén modes in a fusion device is concluded in Sec. VI along with suggestions for future work.

II. SHEAR ALFVÉN WAVE IN LAPD

A. Review of LAPD Alfvén wave studies

The LAPD is ideal for studying SAW because its large physical size, and sufficiently high plasma density and magnetic field, allow it to accommodate multiple Alfven wavelengths. Research on SAW properties in the LAPD dates back to 1994 when a pair of theoretical[22,23] and experimental[24,25] papers were published on SAWs radiated from small perpendicular scale sources in the LAPD. Subsequently, other mechanisms were discovered to generate Alfvén waves including a variety of inserted antennas, resonance between the LAPD cathode, and the semitransparent anode—the Alfvén maser,[26] and a dense laser-produced plasma expansion.[27]

Two regimes of plasma parameters for SAW propagation have been investigated for the cylindrical LAPD plasma with uniform axial magnetic field: the kinetic Alfvén wave (KAW) for plasma electrons having a Boltzmann distribution in the presence of the Alfvén wave fields and the inertial Alfvén wave (IAW) for electrons responding inertially to the wave. The KAW is more relevant to the physics of the interior regions of tokamak plasmas and the IAW to the edge and limiter regions. A dimensionless parameter, $\bar{\beta}_e \equiv \bar{v}_{te}^2/v_A^2$ is a quantitative measure of how inertial or kinetic a plasma region is, where $\bar{v}_{te}=\sqrt{2T_e/m_e}$ is the thermal electron speed with T_e the electron temperature. If $\bar{\beta}_e \gg 1$, the region is kinetic; if $\bar{\beta}_e \ll 1$, then it is inertial. For most of the plasma conditions in this work $\bar{\beta}_e \approx 1$, which implies that SAW propagation features are a mixture of both the KAW and the IAW. The standard magnetohydrodynamic (MHD) SAW dispersion relation is

$$k_{\parallel}^2 c^2 = \frac{\omega^2 \omega_{pi}^2}{\omega_{ci}^2-\omega^2} - \frac{1}{2}k_{\perp}^2 c^2 + \sqrt{\frac{1}{4}k_{\perp}^4 c^4 + \frac{\omega_{pi}^4}{(\omega_{ci}^2-\omega^2)^2}\frac{\omega^6}{\omega_{ci}^2}}, \tag{2}$$

which can be reduced to the following form in the limit of $k_{\parallel} \ll k_{\perp}$:

$$\omega^2/k_{\parallel}^2 = v_A^2(1-\bar{\omega}^2), \tag{3}$$

where $\bar{\omega}=\omega/\omega_{ci}$ and $k_{\parallel}$ is the component of the wave vector parallel to the background magnetic field. The corrections to the dispersion relation for the KAW are proportional to $k_{\perp}^2\rho_s^2$, where $k_{\perp}$ is the perpendicular wave number and ρ_s is the ion sound gyroradius $\rho_s=c_s/\omega_{ci}$ with $c_s=(T_e/m_i)^{1/2}$. The IAW correction is proportional to $k_{\perp}^2\delta_e^2$, where δ_e is the electron skin depth, $\delta_e=c/\omega_{pe}$ with $\omega_{pe}=\sqrt{n_e e^2/\varepsilon_0 m_e}$ as the plasma frequency. In this experimental work, both correction factors are on the order of 0.1 and thus negligible.

An important departure from MHD is that a component of the wave electric field may be sustained parallel to $\mathbf{B}_0$ due to finite electron pressure (KAW) or inertia (IAW). This parallel electric field can lead to energization of the background electrons and thus excite the wave, which can be done by direct application of an oscillating charge density to a flat, circular mesh "disk antenna"[24,26] within the plasma, or it may be excited inductively using a "blade antenna"[30,31] which is an externally fed current with one leg within the plasma parallel to the background field. For either excitation mechanism, there are some general characteristics of the radiated wave field patterns which may be illustrated by considering the disk exciter in detail. Within or close to the inertial regime, a single SAW cone can be excited from both antennas. Assuming azimuthal symmetry, the wave magnetic field has one dominant component $\tilde{B}_\theta$ as a function of r and z,

$$\tilde{B}_\theta \propto \frac{I_{\text{ant}}}{a}\int_0^\infty dk_{\perp}\frac{\sin k_{\perp}a}{k_{\perp}}J_1(k_{\perp}r)\exp[ik_{\parallel}z], \tag{4}$$

in which I_{ant} is the antenna current amplitude and a is the radius of the antenna cross section. There are three characteristic features of the radial profiles:[22,24] (1) the field is always zero at the disk center; (2) it increases with the radial distance away from the disk center until reaching a peak value, the radial location of which increases with axial distance away from the exciter; (3) upon reaching the position, r_{edge} (the location of the outer Alfvén cone), defined by

$$r_{\text{edge}} = \left(\frac{\omega}{v_A}\delta_e z/\sqrt{1-\bar{\omega}^2}\right) + a, \tag{5}$$

the wave magnetic field decreases as $1/r$.

A total of three different antenna designs are used in this experiment to generate SAWs with different azimuthal mode numbers (m) (Fig. 2 below). For $m=0$, the disk antenna is the standard small source with a diameter (1.0 cm) comparable to the electron skin depth ($\delta_e \sim 0.5$ cm). A phase locked rf tone burst at a variable frequency (below the minimum cyclotron frequency at B_0) is fed to the positively biased disk to drive SAW. The field aligned blade antenna is made of a solid copper cylinder 0.96 cm in diameter. A sinusoidal rf current of ~2.0 A (rms) flows in the long leg aligned along z axis and azimuthally inductively coupled to the plasma with minimal influences from the two radial legs. To launch an $m=1$ mode, a rectangular loop antenna containing two parallel current channels can be used. The resulting field pattern resembles two small disk or blade antennas separated by a small distance only in perpendicular plane and driven with currents 180° out of phase.[28,29] Two intersecting Alfvén cone structures constructively interfere with each other to form a linearly polarized wave field propagating through the loop antenna axis that also aligns with the background magnetic field. Due to the simplicity of $m=0$, the field aligned blade antenna and the small disk antenna are most frequently used in this work.

A number of previous studies on Alfvén modes were conducted in the LAPD plasma with different boundary conditions, the results of which this experimental work benefits from. Mitchell *et al.*[30,31] in 2001 used an impulsive driving current to study the field-line-resonance spectra for a constant magnetic field with strong reflective boundary conditions (a conductive end-plate at one end and the anode/cathode at the other end). A series of field-line-resonance eigenmodes were discovered having frequencies proportional to Alfvén velocity and inversely proportional to the length of the machine with the finite ion cyclotron frequency correction. Later the same year, Vincena *et al.*[32] created a section ($\sim$3 m) of magnetic field gradient in the center of the LAPD and studied Alfvén wave propagation in both parallel and perpendicular directions. Upon reaching the cyclotron resonance location in the magnetic field gradient, the wave was almost completely absorbed with no reflection observed. A WKB model was used to find the ray of wave group velocity vectors and estimate the major damping mechanisms. Soon after in 2002, Mitchell *et al.*[33] expanded the magnetic field gradient to $\sim$9 m and perpendicular SAW refraction was characterized as the Alfvén wave traveled from the KAW ($\bar{\beta}_e \approx 10$) to the IAW ($\bar{\beta}_e \approx 0.003$) region.

B. Analytical estimate of the spectral gap

In this section, the expected generation of the spectral gap by a magnetic mirror array field is estimated from the electromagnetic wave equations. Consider a periodic magnetic field given by

$$B_{0z} = \frac{B_{\max}+B_{\min}}{2}\left[1 - M\cos\left(\frac{2\pi}{L_m}z\right)\right], \tag{6}$$

where L_m is the mirror length and $M=(B_{\max}-B_{\min})/(B_{\max}+B_{\min})$ is the mirror depth. The refraction index for the SAW is

$$N^2 = \frac{c^2}{v_A^2} = \frac{n_i m_i}{B_{0z}^2 \varepsilon_0} \gg 1, \tag{7}$$

where c is the speed of light and ε_0 is the vacuum permittivity. Substituting Eq. (6) into Eq. (7) gives

$$N^2 = \frac{4 n_i m_i}{(B_{\max}+B_{\min})^2 \varepsilon_0}\frac{1}{\left[1 - M\cos\left(\frac{2\pi}{L_m}z\right)\right]^2} \sim \frac{\varepsilon_p}{\varepsilon_0}\left[1 + 2M\cos\left(\frac{2\pi}{L_m}z\right)\right], \tag{8}$$

for weak modulation amplitude ($M \ll 1$), where $\varepsilon_p \equiv 4 n_i m_i/(B_{\max}+B_{\min})^2$.

The wave equation for the transverse electric wave field is

$$\nabla_\parallel^2 E_y(z) + \omega^2 \mu_0 \varepsilon_0 N^2 E_y(z) = 0. \tag{9}$$

The magnetic field can be obtained from Maxwell's equations. Using a dimensionless variable $\xi = \pi z/L_m$, Eq. (9) is cast into the form of the canonical Mathieu's equation,[34]

$$\frac{d^2}{d\xi^2}E_y + [a - 2q\cos(2\xi)]E_y = 0, \tag{10}$$

where the two coefficients are, respectively,

$$\begin{aligned} a &= \left(\frac{L_m}{\pi}\right)^2 (\omega^2 \mu_0 \varepsilon_p) = \left(\frac{f}{f_{\text{Bragg}}}\right)^2, \\ q &= -\left(\frac{L_m}{\pi}\right)^2 (\omega^2 \mu_0 \varepsilon_p) M = -aM. \end{aligned} \tag{11}$$

The ideal Bragg frequency is defined as $f_{\text{Bragg}} = \bar{v}_A/2L_m$, at which the Bragg condition is satisfied and the wave propagation is suppressed by multiple reflections from the mirror cells. Here the average Alfvén speed $\bar{v}_A$ is used and $k_{\text{Bragg}} = \pi/L_m$. Using the power series for a and q from Ref. 30, with mode number $n=1$, there are two branches of solutions as

$$a_+ = 1 - q - \frac{q^2}{8}\cdots, \quad a_- = 1 + q - \frac{q^2}{8}\cdots. \tag{12}$$

Dropping the nonlinear terms and solving for the upper and lower continuum eigenfrequencies by inserting Eq. (10) into Eq. (11) gives

$$\frac{f_+}{f_{\text{Bragg}}} = \sqrt{\frac{1}{1-M}}, \quad \frac{f_-}{f_{\text{Bragg}}} = \sqrt{\frac{1}{1+M}}. \tag{13}$$

Thus the width of the SAW spectral gap is

$$\Delta f = f_+ - f_- \approx M f_{\text{Bragg}}, \tag{14}$$

which varies linearly with the field modulation amplitude M of an infinite magnetic mirror array. There are two major premises for this result: infinite number of mirror cells and a much-less-than-unity M—both are experimentally difficult to implement. Nevertheless, Eq. (14) provides qualitative guidance for the following experimental studies.

An alternative treatment of this problem also reveals that the coupling between the forward and backward waves causes the spectral gap just as in other physical environments. In the case of shear Alfvén waves propagating parallel to a constant magnetic field, the dispersion relations for forward and backward waves are $\omega_\pm = \pm k_\parallel v_A$. If the backward wave is purely contributed by reflections from a periodic magnetic mirror array, the dispersion relation is modified to be $\omega_- = -(k_\parallel - 2k_{\text{Bragg}})v_A$ in order to satisfy the conservation of momentum. They are shown as two intersecting lines in a $\omega - k_\parallel$ plot as in Fig. 1. The coupling of these two waves can be formally described by equating the product of their dispersion relations with a coupling term CT,[35]

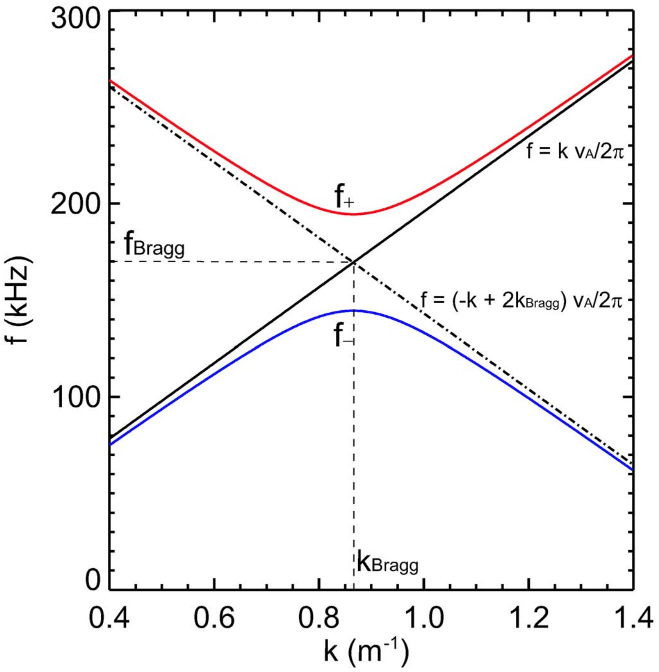

FIG. 1. (Color online) Illustration of coupled shear Alfvén wave in an infinite magnetic mirror array configuration. Parameters used for calculation are: $CT=(2\pi\times 25\times 10^3)^2\ s^{-2}$, $L_m=3.63$ m, $v_A=1.23\times 10^6$ m/s.

$$(\omega - k_{\parallel}v_A)\times[\omega + (k_{\parallel}-2k_{\text{Bragg}})v_A] = \text{CT}. \qquad (15)$$

Solving for ω yields two similar branches of solutions:

$$\omega_{\pm} = k_{\text{Bragg}}v_A \pm \sqrt{(k_{\parallel}-k_{\text{Bragg}})^2 v_A^2 + \text{CT}}. \qquad (16)$$

At the Bragg condition, $k=k_{\text{Bragg}}$, this frequency gap is given by

$$\Delta\omega = 2\sqrt{\text{CT}}. \qquad (17)$$

Choosing a specific value for $\text{CT}\sim\omega_+^2$, a coupled dispersion relation is plotted in Fig. 1, which demonstrates both the forbidden gap and the forward and reflected branches *at* $k=k_{\text{Bragg}}$.

III. EXPERIMENTAL SETUP

A. Magnetic mirror array in the LAPD

The experimental part of this work is performed in the upgraded LAPD, which has a 17.56-m-long, 1-m-diam cylindrical main vacuum chamber surrounded by ten sets of pancake electromagnets (90 in total) fed by ten independent power supplies—this offers a maximum of five magnetic mirror cells (each cell requires two sets of magnets). Pulsed plasmas (~10 ms in duration, 1 Hz repetition rate and ±10% spatial uniformity) are created by electron discharge between a barium oxide coated cathode and a semitransparent molybdenum anode.[36] The cathode and anode are separated by 50 cm and are both located at the south end of the machine. Typical average plasma parameters are $n_i\sim 1\times 10^{12}\ \text{cm}^{-3}$, $T_e\sim 6$ eV, $T_i\sim 1.0\pm 0.5$ eV. The low plasma density is chosen to avoid strong Alfvén maser formation[26] as a major source of wave field noise. The working gas is helium at a partial pressure $\sim 1.6\times 10^{-6}$ Torr with less than 3% of impurities.

Figure 2 shows the baseline mirror array configuration ($M=0.25$) for this experiment together with the axial arrangement of SAW antennas and plasma/wave diagnostics. This figure serves as a reference of relative z positions for the port numbers mentioned throughout this paper. The two sets of magnets next to the anode-cathode (south) are both carrying the higher current corresponding to a 1.5 kG field to sustain a steady plasma discharge, which leaves four and a half mirror cells available to form the array. A strong dissipating magnetic beach on the north end of the machine was initially included in the mirror array field design to suppress the cavity modes that would otherwise overlap with multiple-mirror induced modes. The axial magnetic field profiles are calculated from the actual current distribution for all the magnets in the machine.[37] The estimated axial field ripple amplitude at the radius of the machine is less than 2% for a constant field configuration.

Since the LAPD was not previously diagnosed for a magnetic mirror array, plasma parameter (n_i,T_e) profiles from triple Langmuir probe scans are examined before and monitored during the SAW experiment to ensure that the plasma column is only slightly perturbed by the mirror field. Chamber-wide (1 cm step for 96 cm) line scans along the x axis (Fig. 2) are taken at ports 13, 15, 19, and 35 with the baseline mirror array configuration ($M=0.25$). A stationary 56 GHz interferometer at port 23 measures the real time line-integrated plasma density which is used to calibrate triple probe data. Plasma density and temperature data are then used to calculate the thermal electron velocity, the local Alfvén speed and $\bar{\beta}_e$. Figure 3 shows the calculated quantities along a horizontal line ($y=0$) to represent the radial profiles assuming azimuthal symmetry. Comparing data of port 19 ($B_{0\ \max}$) to port 13 ($B_{0\ \min}$), the difference in v_A and $\bar{\beta}_e$ are due to the difference in local magnetic field. Port 35 ($B_{0\ \min}$) data are also plotted next to those of port 13 ($B_{0\ \max}$) to demonstrate the plasma uniformity along the z axis. $\bar{\beta}_e$ alternates to be above and below 1.0 as the external B field changes between $B_{0\ \min}$ and $B_{0\ \max}$, which implies that the shear Alfvén waves alternate between the kinetic ($\bar{\beta}_e>1$) and the inertial ($\bar{\beta}_e<1$) regime.

B. Launching SAW in a magnetic mirror array

As depicted in Fig. 2, three different antennas are individually placed at the radial center of the cylindrical plasma column where the axial location of each antenna is defined to be $z=0$ for each probe. The advantage of studying axial (parallel) periodicity-induced SAW spectra with various antennas and launching mechanisms is to exclude any spectral features controlled by the physical characteristics of the antenna. The disk and rectangular loop antenna are used only for preliminary studies of this work and the spectral results are similar to those using the blade antenna. Unless otherwise specified, all experiment results here are from the blade antenna.

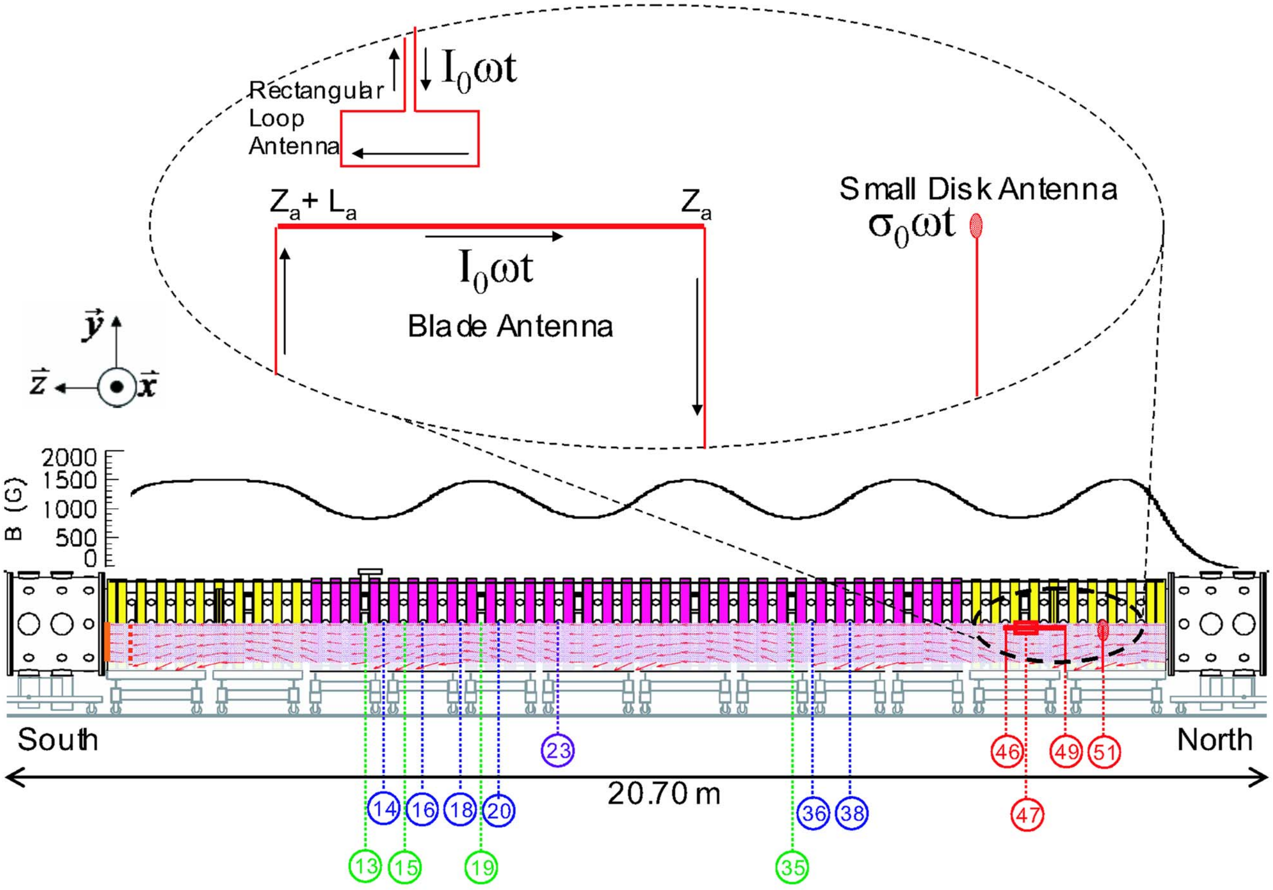

FIG. 2. (Color online) Side view of the baseline mirror array configuration ($M=0.25$) at the LAPD (lower half of the chamber is semitransparent). Red arrows illustrate the vectors (not to scale) of the mirror magnetic field. Circled numbers indicate port numbers of inserted instruments. Axial distance between two adjacent ports is 0.32 m. Port 23: Microwave interferometers for column integrated plasma density calibration; Port 13, 15, 19, 35: Triple probes for local T_e, n_i measurements; Port 51: SAW small disk antenna; Port 46–49: SAW blade antenna; Port 47: rectangular loop antenna; Port 14, 16, 18, 20, 36, 38: B-dot probes for local SAW magnetic field measurements.

During the experiment, the SAW antenna is driven by a rf sine wave train of ~200 periods at one frequency for a desired number of shots before changing to the next frequency. A frequency scan from 75 kHz to 275 kHz with a step size of 5 kHz is typical. The antenna current is found to be frequency dependent, steadily decreasing from 8.5 A at 25 kHz to 2.0 A at 325 kHz (Fig. 6 below). Measurements of the forward and reflected power show that resonances in antenna coupling are absent over this frequency range. When the magnetic wave field is analyzed as a function of frequency, the antenna current variation is accounted for using a modified cross-covariance technique to be introduced below.

C. SAW signal detection and processing

The wave magnetic field is measured by a set of ten identical *B-dot* probes featuring three orthogonally oriented induction coil-pairs which are sensitive to the time derivative of the wave magnetic field.[38] Each coil-pair is connected to a differential amplifier to select magnetic signal and reject common mode noise. During the experiments, the magnetic coils are oriented so that the three components of the wave field align with the coordinate system in Fig. 2. For each SAW launching frequency and axial (z) location, measurements are taken every 1 cm along a radial line (typically the x axis). After signal averaging over a number of plasma shots, the probe tip is moved to the next radial position and the process is repeated.

After being digitized and saved as data time sequences, the SAW antenna current I_{ant} and the three components of the SAW field ($\tilde{B}_i$ as the ith component) signals are processed using a cross-covariance algorithm,

$$\langle \tilde{B}_i(L)\rangle = \frac{\sum_{k=0}^{N-|L|-1}(\tilde{B}_{i\ k+|L|}-\bar{\tilde{B}}_i)(I_{\mathrm{ant}\ k}-\bar{I}_{\mathrm{ant}})}{\sqrt{\sum_{k=0}^{N-1}(I_{\mathrm{ant}\ k}-\bar{I}_{\mathrm{ant}})^2/N}}, \quad L<0, \tag{18}$$

where N is the length of the array, L is a variable lag between $\tilde{B}_i$ and I_{ant}, $\bar{\tilde{B}}$ and $\bar{I}_{\mathrm{ant}}$ are the averaged rms values. Here, k represents the index of the time-sequence array. After scanning to a sufficiently large L, the lag that yields the first maximum of the cross-covariance is interpreted as the propagation time of the wave between the antenna and the detector. The resulting maximum $\langle \tilde{B}_i\rangle$ is close to its rms value within 5%. In the following discussion, $\tilde{B}_\theta$ is used to represent the SAW magnetic field acquired using the aforemen-

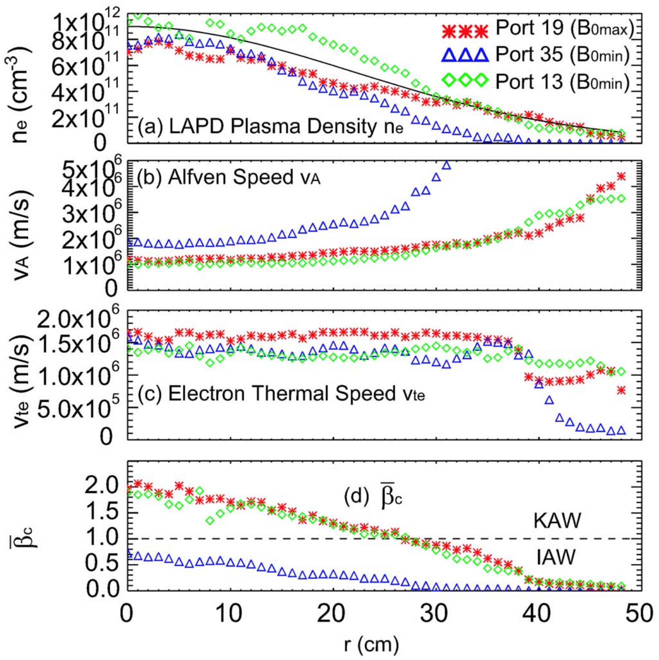

FIG. 3. (Color online) Radial profiles of (a) the plasma density $n_e \sim n_i$, solid curve is a fit using $n(r) = 9\times10^{11}\exp[-1.02\times10^{-3}r^2]$ cm^{-3}; (b) the Alfvén speed v_A; (c) the electron thermal speed v_{te}; and (d) $\bar{\beta}_e$, dashed line shows $\bar{\beta}_e = 1$. All in the LAPD baseline mirror array configuration ($M = 0.25$). Triple probe data including n_i and T_e are acquired with 50 MHz sampling rate of the digitizer, averaging 128 samples and 10 plasma shots. Random error <10%.

tioned technique. Relative wave amplitudes ($\tilde{B}_\theta / B_0$) of up to 10^{-4} are observed 3.2 m away from the antenna, which is approximately half a SAW wavelength (near field influence range) in uniform field LAPD plasma with an intermediate frequency. The wave activity is in the linear response regime, which is a precondition for the following discussions of spectral features.

Figure 4 shows typical $\tilde{B}_\theta$ amplitude (averaged over 0.02 ms) radial profiles at port 14 (axial distance from the antenna south end to the probe $\Delta z = 10.24$ m) comparing two background field configurations: uniform field and baseline mirror array configuration ($M = 0.25$). These profiles match the prediction of Eq. (4) with peak wave field amplitude ~5 cm away from the minimum. With the magnetic mirror array, the wave field drops drastically near $f_{\mathrm{Bragg}} \sim 159$ kHz ($L \sim 3.63$ m).

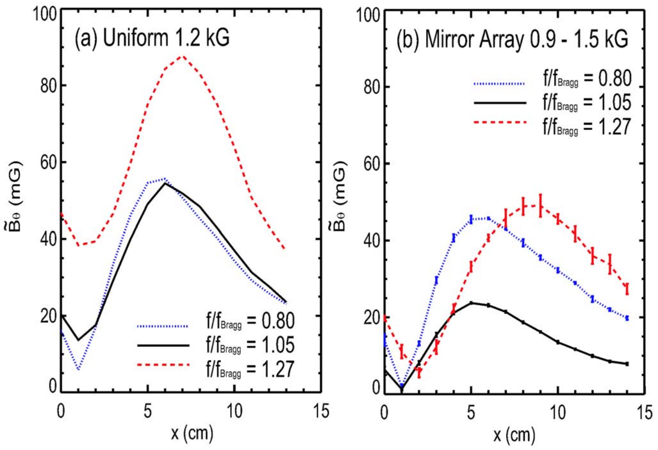

FIG. 4. (Color online) $\tilde{B}_\theta$ radial profiles at $\Delta z = 10.24$ m (port 14): (a) uniform magnetic field 1.2 kG, average $n_e = 2.0\times10^{12}$ cm^{-3}, $f_{\mathrm{Bragg}} = 124$ kHz; (b) baseline mirror array configuration ($M = 0.25$), 0.9–1.5 kG, average $n_e = 1.0\times10^{12}$ cm^{-3}, $f_{\mathrm{Bragg}} = 160$ kHz. [Field amplitude data acquired with 100 MHz sampling rate, averaging eight samples. (b) shows error bars calculated from five consecutive plasma shots.]

IV. SPECTRAL RESULTS

A. Characteristics of wave spectra

In the following sections, the spectral intensity observed at various axial points and transverse to the magnetic field are plotted as a function of frequency. In a cylindrical system, U is defined as the wave magnetic energy density integrated over the azimuthal and radial coordinates,

$$U = \pi\mu_0\left[\int_0^{r_{\mathrm{edge}}}\tilde{B}_\theta(r)^2 r\,dr + b_{\mathrm{edge}}^2 \ln(r)\Big|_{r_{\mathrm{edge}}}^{r_{\mathrm{plasma}}}\right], \qquad (19)$$

where b_{edge} is the magnitude of wave magnetic field at the Alfvén cone edge r_{edge} and $r_{\mathrm{plasma}} \sim 30$ cm is the average radius of the plasma column. Since $U\Delta z$ yields the total wave magnetic energy of a thin disk at one axial location, U can be also referred to as the "disk energy density."[39]

In practice, a *B-dot* probe data scan at one axial position covers radially from 0 to 14 cm at a stepping of 1 cm. This range includes the peak of $\tilde{B}_\theta(r)$ and part of the $1/r$ falling tail. b_{edge} can be reasonably replaced by the $\tilde{B}_\theta(r)$ value at $r = 14$ cm.

The ideal Bragg frequency is used to normalize the frequency. There are two error sources for estimating f_{Bragg}. First, the number of mirror cells is not infinite as the Bragg theory requires. Having as many mirror cells as possible is again important in this sense. Second, the value of the average Alfvén speed $\bar{v}_A$ has some uncertainty. Here, $\bar{v}_A$ is calculated two ways: (1) by using the average plasma density and magnetic field in the $\bar{v}_A$ formula and (2) by dividing the wave travel distance by the launch-detection delay time acquired from the cross-covariance analysis. The average of both methods is used and they usually agree with each other to within 10%.

B. Dependence of the wave propagation characteristics on the number of mirror cells

The existence of the mirror-induced SAW spectral gap was first observed in the experimental results shown in Fig. 5, where the wave spectra for various mirror configurations are plotted: from zero (uniform field) to four mirror cells. The small disk antenna is placed at port 51, defining the $z = 0$ position. A *B-dot* probe is inserted in port 14 ($z = 11.80$ m) and radial scans are taken with SAW frequency swept from 50 kHz to 180 kHz at intervals of 5 kHz. The wave spectral intensity is the maximum field amplitude $\tilde{B}_\theta(r)$ of each radial wave field profile. The spectral gap becomes evident for the four-mirror configuration where the wave field amplitude forms a trough near f_{Bragg} (~120 kHz). At higher frequencies above 150 kHz, the shaded area corre-

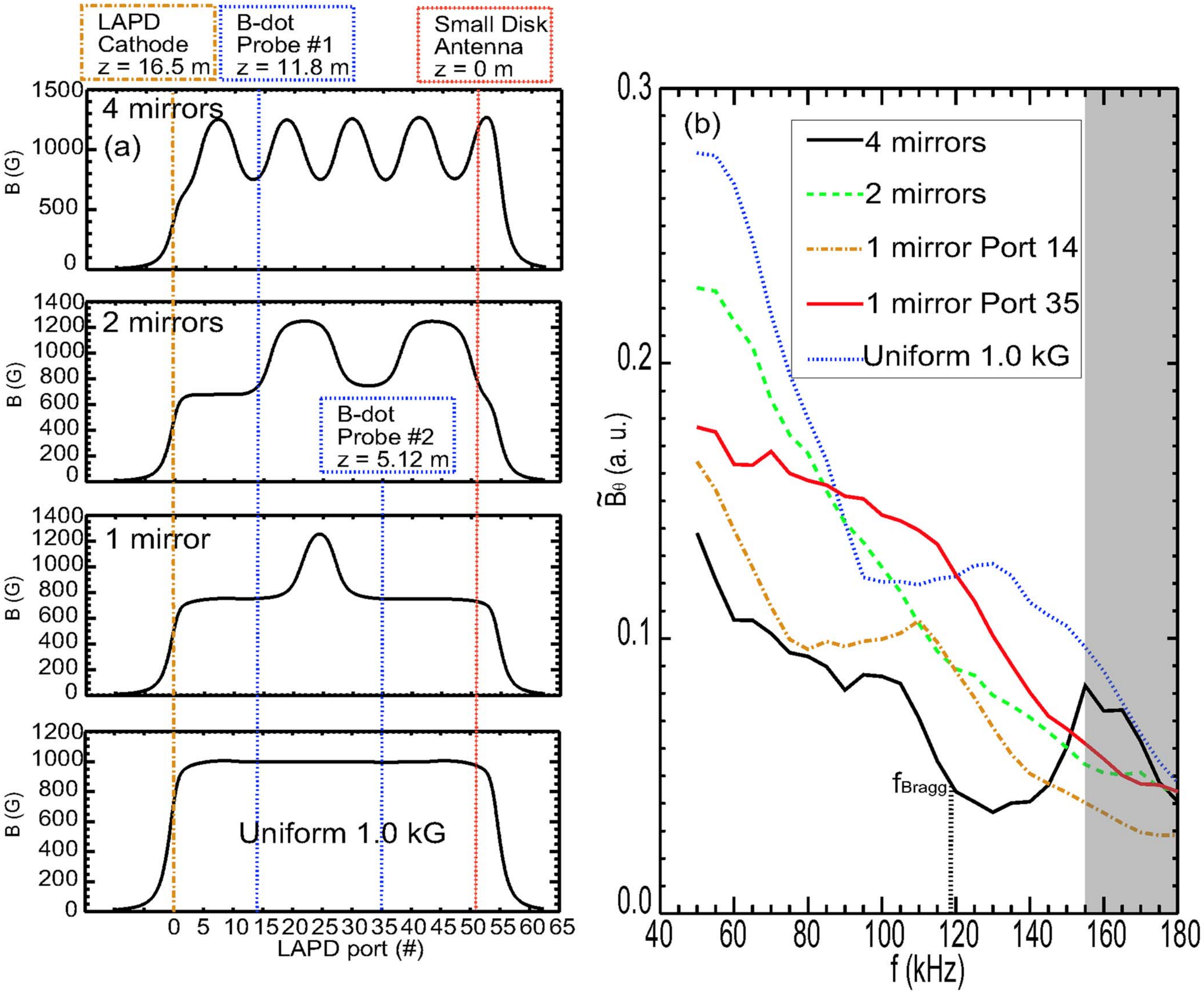

FIG. 5. (Color online) SAW spectra with various numbers of mirror cells in the LAPD. (a) Magnetic mirror configurations including the uniform case, where the axial magnetic field is plotted against the LAPD port number. (Axial distance between two adjacent ports is 0.32 m.) (b) $\tilde{B}_\theta$ vs SAW frequency, curves labeled according to the mirror array configuration. (Field amplitude data acquired with 100 MHz sampling rate, averaging eight samples and 16 consecutive plasma shots. Maximum vertical error is less than 10% and horizontal ±1 kHz.)

sponds to a large underestimate of field amplitude since these earlier radial scans were taken up to $r=10$ cm and the peak amplitude of high frequencies were left out. Nevertheless, this test shows that the spectral gap feature arises when there are a sufficient number of periods in the mirror array configuration.

C. Characteristics of spectral gap and continua

With expanded radial scan range (up to $r=14$ cm) and frequency scan range (75–275 kHz), distinct spectral gap and two continua next to the gap can now be studied in detail. Figure 6 shows the SAW field spectrum for the baseline mirror array configuration ($M=0.25$). In Fig. 6(a) the radial-peak magnetic field and (b) the "disk energy density" are plotted versus the normalized frequency (f/f_{Bragg}). Both plots reveal the gap and two continua distinctly but the "disk energy density" spectrum has a better contrast between the peak and trough in addition to its better physical representation of the spectral intensity. Also in Fig. 6(a), the current in the antenna is frequency dependent but there are clearly no resonances. Here some spectral features are defined for future discussions: f_G and $f_{+(-)}$ are in turn the gap center frequency and the upper (lower) continuum frequency; the spectral intensity at f_G is defined as U_G and $U_{+(-)}$ at $f_{+(-)}$; the spectral full-width-at-half-maximum (FWHM) at $f_{+(-)}$ is defined as $\gamma_{+(-)}$; the spectral gap width Δf_G is the difference between f_+ and f_-.

D. Varying mirror depth (*M*)

In order to verify the dependence of SAW spectral gap width (Δf) on the mirror depth (M), four mirror array configurations are tested in the LAPD with different magnetic mirror depths (Fig. 7). The axially aligned blade SAW antenna extends from port 46 to port 49 for about 96 cm. The

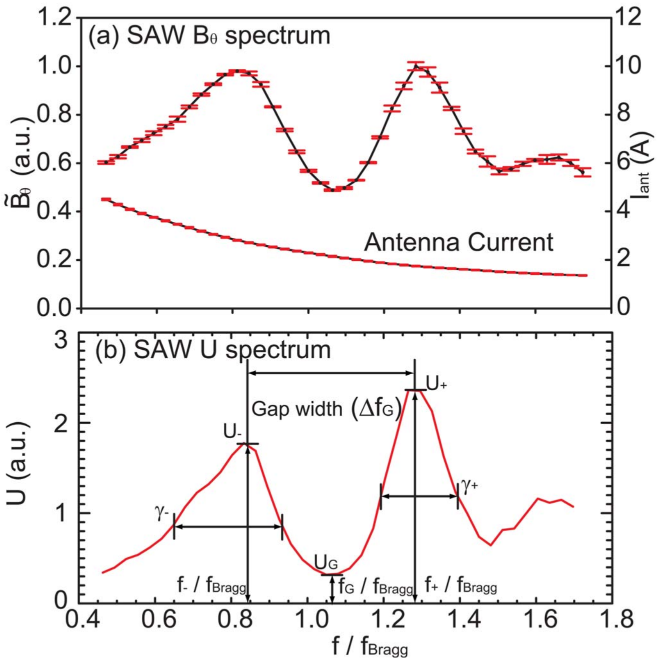

FIG. 6. (Color online) Two different representations of the SAW spectrum at port 14 with the baseline mirror configuration ($M=0.25$). (a) Normalized $\tilde{B}_\theta$ vs f/f_{Bragg}; antenna current rms value is also overplotted (error bars may be too small to be distinguished from the curve); (b) "disk energy density" normalized using a constant $(1.0\times 10^5/\mu_0\pi)$ vs f/f_{Bragg}. $f_{\text{Bragg}}=160$ kHz. (All data acquired with 100 MHz sampling rate, averaging eight samples and five consecutive plasma shots. Maximum horizontal error is ±0.01.)

LAPD anode/cathode set is located 14 m away to the south of port 46, which provides a strong reflective boundary condition.[30,31] At the north end of the machine, a 2.6 m long magnetic beach is presented for all configurations for a strong absorbing boundary condition. A *B-dot* probe is inserted in port 14 ($z=10.24$ m) for radial scans. Notice that the background magnetic field configuration to the south of port 14 is kept constant for all mirror depths in order to preserve both a steady performance of the LAPD discharge and a steady plasma environment for the SAW diagnostics.

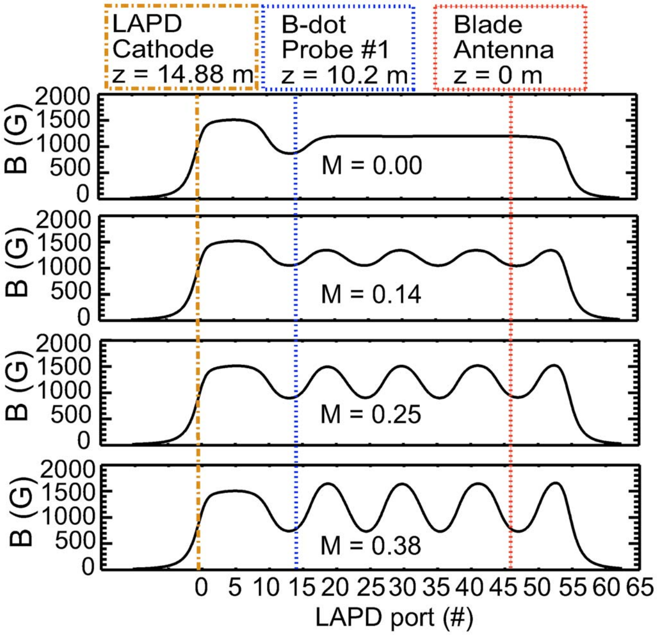

FIG. 7. (Color online) Four magnetic mirror array configurations with gradually increased mirror depth. (M calculated with B field from port 20 to port 53; axial distance between two adjacent ports is 0.32 m.)

The resulting spectra from all four mirror array settings are shown in Fig. 8 where the gap width gradually increases with the mirror depth. Although each mirror array configuration has different plasma density and thus different v_A, the mirror array spectra (normalized to f_{Bragg}) have a nearly identical gap center at $f/f_{\text{Bragg}}\sim 1.05$. With the uniform 1.2 kG magnetic field, there is only one spectral peak that splits into two branches once M is increased above zero.

The dependence of the normalized spectral gap width $(\Delta f_G/f_G)$ on the magnetic mirror depth (M) is shown in Fig. 9(a). In both experiment and simulation (see Sec. V C), the spectral gap width increases with the mirror depth. The agreement between the experiment and the simulation is good for both small and large values of M. As M goes significantly above 0.1, the gap width deviates from the linear dependence predicted analytically in the small M limit [Eq. (14)]. The gap width is larger than the prediction in both experiment and simulation. Simulations with an infinite number of mirror cells (Sec. V B) agree well with Eq. (14), showing that this difference is caused by the finite number of mirror cells in the experiment. The transmitted wave field amplitude and disk energy density at f_G are shown in Fig. 9(b). It is noticeable that the spectral intensity at the gap center decreases with higher M, which suggests higher modulation strength in a periodic system cause higher reflectivity of the wave.

E. Verification: Interference causes spectral gap

It is interesting to examine how the spectral features come into being over time. All previous data analysis is done with rf magnetic field response averaged over ~0.2 ms containing 15 full wave cycles for the lowest launching frequency (75 kHz). To have the best temporal resolution, the cross-covariance analysis averages over one wave period of each SAW frequency and progresses at a small time step (0.2 μs) forward from the onset of the antenna current signal. The temporal resolution is determined roughly by the order of the wave period so that the higher frequency has better resolution (up to 3.6 μs). The contour plot in Fig. 10(a) shows the wave field amplitude versus frequency and time in order to reveal the onset of mirror array-induced spectral features. The left curve shows the time that it takes the wave front to propagate from the antenna to the *B-dot* probe the first time, calculated from dividing the axial distance (10.24 m) by the parallel group velocity in the cold-plasma (black solid) approximation. The curvature agrees with the contour plot in that the higher frequency SAW travels with slower group velocity in the parallel direction. It is important to notice that, before the wave is reflected back from the anode/cathode, the gap and continua features are already formed, which shows that the mirror cells alone can cause strong modification of the spectrum. The features then grow to the fullest contrast upon reaching the curve to the

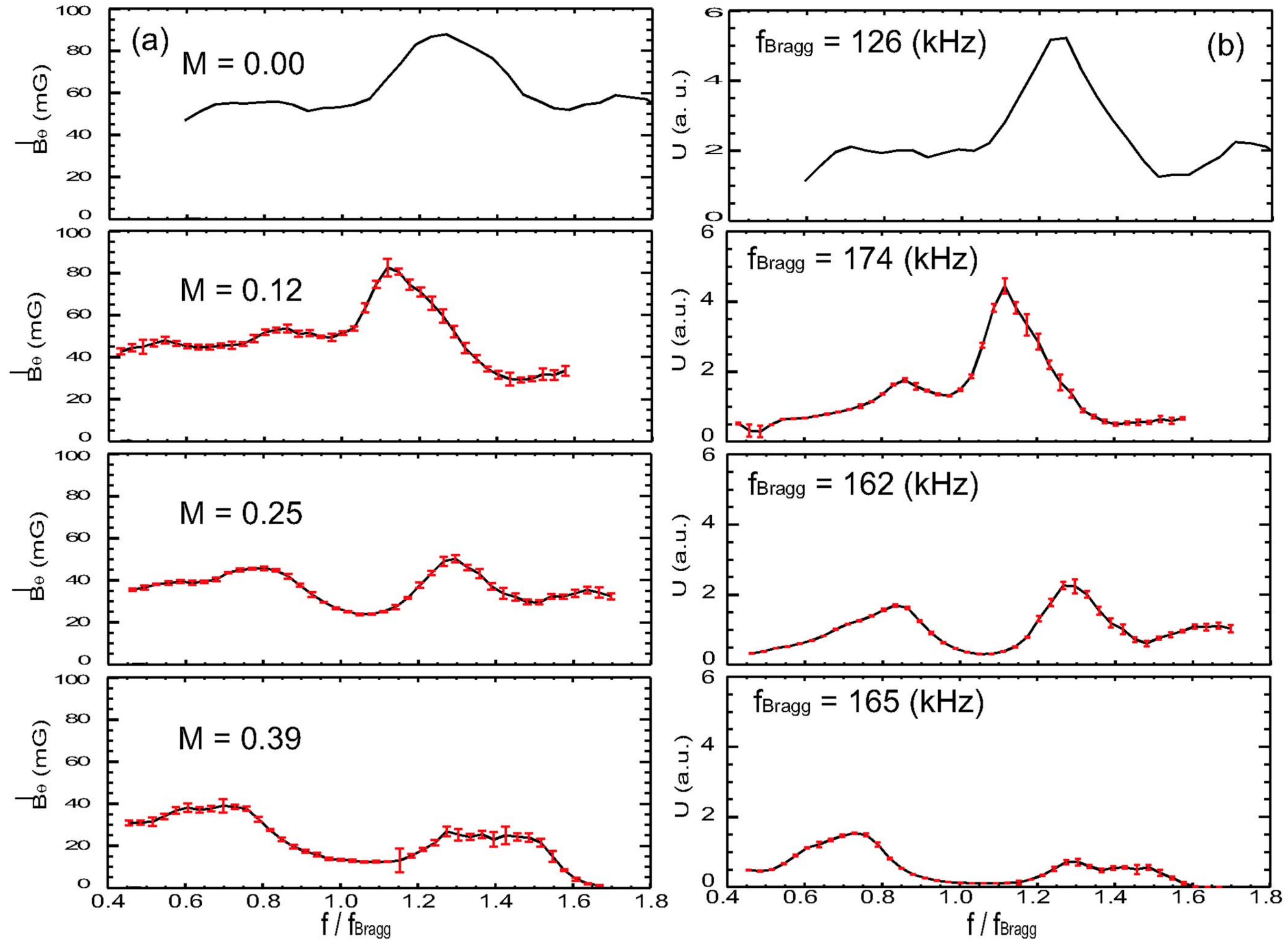

FIG. 8. (Color online) SAW spectra for four magnetic mirror array configurations with different mirror depth (M) at port 14: (a) maximum $\tilde{B}_\theta(r)$ vs f/f_{Bragg} and (b) "disk energy density" normalized using a constant $(1.0\times 10^5/\mu_0\pi)$ vs f/f_{Bragg}. Vertical error bars calculated from five consecutive plasma shots. Maximum horizontal error is ±0.01.

right, which is the time that it takes the wave to reflect from the anode/cathode and back to port 14, again calculated from the dispersion relation. From Fig. 10(b), where the wave field amplitudes are plotted against time for three characteristic frequencies (f_G, f_+, and f_-), it is obvious that the wave amplitude at the gap frequency f_G peaks when the first forward wave front reflects back ($\sim 16\ \mu$s) and then is further suppressed by the destructive interference between the forward and reflected waves. All the features turn into steady state as seen in the previous sections after the initial 40 μs.

F. Continuum quality factor varying with density

The quality factors of the continuum depend on the damping mechanisms of SAW propagation, the refraction and reflection at each mirror cell as well as the machine end condition. The latter two effects will be included in another paper. Here theoretical damping estimation in a straight field LAPD plasma column is used as the only contribution to the theoretical quality factor. In Ref. 32, SAW damping along the ray path through the background field gradient were determined to be mainly from three mechanisms: the ion-cyclotron damping, the electron Landau damping, and the electron-ion Coulomb collisions. In the baseline mirror array configuration ($M=0.25$), the upper continuum f_+ is lower than $0.6f_{ci}$ at $B_{0\ \mathrm{min}}$, which means that the ion-cyclotron damping is negligible. For a general resonant mode ω, the theoretical quality factor can be expressed as

$$Q = \frac{\omega}{\gamma} = \frac{m_i\omega}{m_e(\nu_{ei}+\nu_{e\text{-Landau}})}\left(\frac{k_\parallel}{k_\perp}\right)^2\left(\frac{\omega_{ci}}{\omega}\right)^2, \tag{20}$$

where ν_{ei} is the electron-ion Coulomb collision rate and $\nu_{e\text{-Landau}} \propto \omega$ is the effective collision frequency for electron Landau damping rate [see Eq. (26)]. Several spectra are taken with various n_e in the LAPD as shown in Fig. 11, where the horizontal axis is the normalized frequency f/f_{Bragg} centered to the upper continuum of each curve. When the density drops from $2.66\times 10^{18}\ \mathrm{m}^{-3}$ to $1.26\times 10^{18}\ \mathrm{m}^{-3}$, the normalized spectral width drops as predicted by Eq. (20) as shown in the inset. It is also noticeable that the spectral intensity at the gap center increases with the higher density, which implies that if there are any modes within the gap region, they are not subject to the continuum damping. More quantitative discussions of mode damping mechanisms will be included in the simulation works of Sec. V.

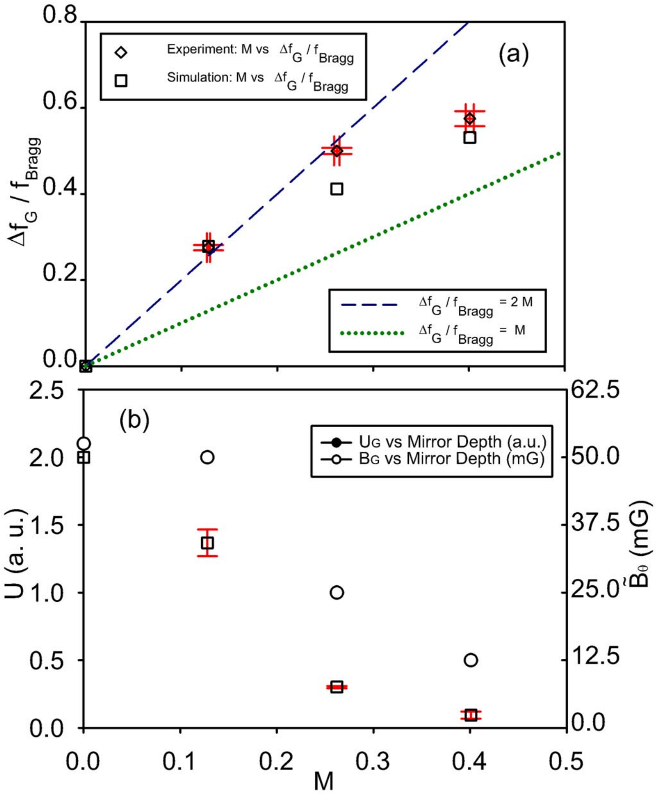

FIG. 9. (Color online) (a) Dependence of spectral gap width on mirror depth (M). Experiment: diamond with error bars; simulation: box; green dotted line: theoretical prediction of Mathieu's equation [Eq. (14)] for an infinite system; blue dashed line: analytical prediction from TAE model (Ref. 44); (b) transmitted wave field amplitude B_G and disk energy density U vs mirror depth (M). (Vertical and horizontal error bars are random errors calculated from five consecutive plasma shots.)

V. SIMULATION

A linear electromagnetic wave solver for cold magnetized plasma is employed to treat a magnetic mirror array configuration. The details of the solver are described in Ref. 40, in which the solver was used to study helicon modes.

A. Electromagnetic wave solver

The wave field is governed by Maxwell's equations in the frequency domain

$$\begin{aligned} &\nabla \times \mathbf{E} = i\omega \mathbf{B}, \\ &\frac{1}{\mu_0}\nabla \times \mathbf{B} = -i\omega \mathbf{D} + \mathbf{j}_a, \end{aligned} \tag{21}$$

where $\mathbf{E}$ and $\mathbf{B}$ are the electric and magnetic fields, μ_0 is the permeability of free space, $\mathbf{D}$ is the electric displacement vector, ω is the antenna frequency, and $\mathbf{j}_a$ is the antenna current density. The cold plasma approximation yields the following relation between the electric displacement vector and the electric field,[41,37]

$$D_{\alpha\beta} = \varepsilon_{\alpha\beta} E_{\alpha\beta},$$

or equivalently

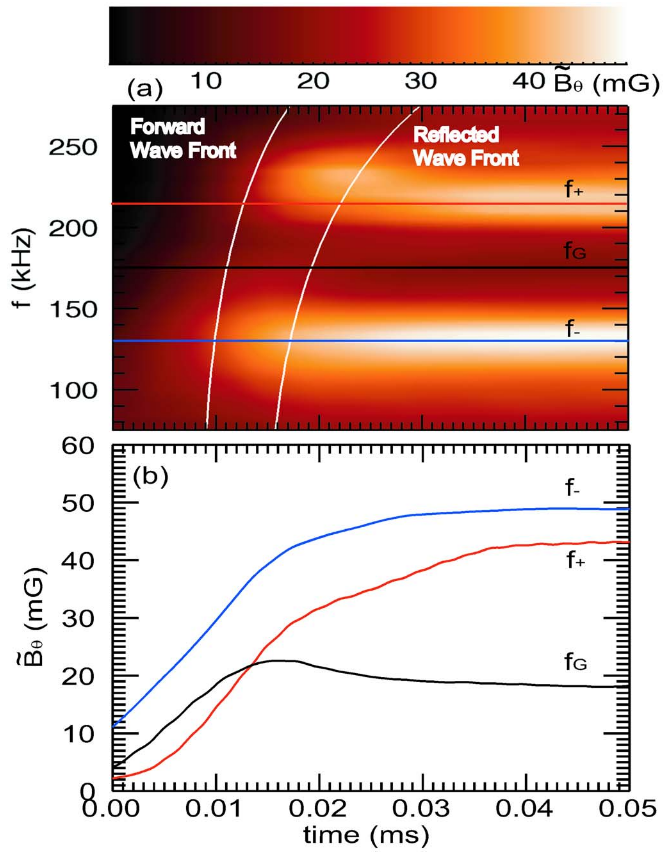

FIG. 10. (Color online) Time history of the running cross-covariance between the wave field and the antenna current with the baseline mirror array configuration (M=0.25) at port 14. (a) Contour plot of wave field intensity vs frequency and time. The first white curve indicates the time that takes the wave to travel towards the probe one-way; the second white curve indicates the time that takes the wave to return to the probe after being reflected at the anode/cathode the first time. (b) Temporal plot of wave field intensity growth at three characteristic frequencies: f_+(215 kHz), f_-(130 kHz), and f_G(175 kHz).

$$\mathbf{D} = \varepsilon_0(\varepsilon \mathbf{E} + ig[\mathbf{E} \times \mathbf{b}] + (\eta - \varepsilon)(\mathbf{E}\cdot\mathbf{b})\mathbf{b}), \tag{22}$$

where $\mathbf{b} \equiv \mathbf{B}_0/B_0$ is the unit vector along the external magnetic field and

$$\begin{aligned} \varepsilon &= 1 - \sum_\alpha \frac{\omega + i\nu_\alpha}{\omega}\frac{\omega_{p\alpha}^2}{(\omega + i\nu_\alpha)^2 - \omega_{c\alpha}^2}, \\ g &= -\sum_\alpha \frac{\omega_{c\alpha}}{\omega}\frac{\omega_{p\alpha}^2}{(\omega + i\nu_\alpha)^2 - \omega_{c\alpha}^2}, \\ \eta &= 1 - \sum_\alpha \frac{\omega_{p\alpha}^2}{\omega(\omega + i\nu_\alpha)}. \end{aligned} \tag{23}$$

Here the subscript α labels particle species (electrons and ions), $\omega_{p\alpha}$ is the plasma frequency, $\omega_{c\alpha}$ is the gyrofrequency, and ν_α is the collision frequency. Singly ionized helium ions are assumed. Equation (21) is solved for a given azimuthal mode number m on a 2D domain (r,z).

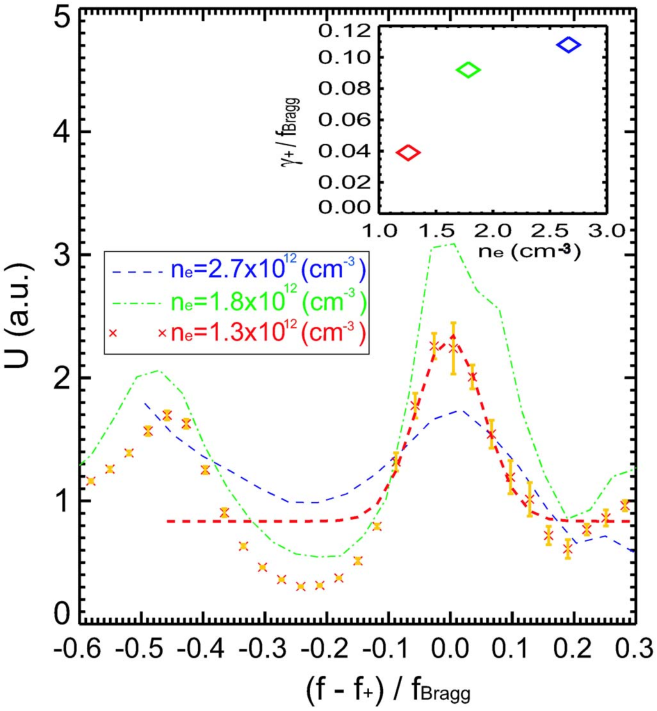

FIG. 11. (Color online) Upper continuum spectra width (γ_+/f_+) with three different plasma densities. The upper continuum of each spectrum is centered at the horizontal origin. The inset shows the normalized spectra width vs plasma density. The error bars as well as the Gaussian fit of the f_+ peak are shown for the $n_e=1.26\times10^{18}$ m^{-3} case. (All data acquired with 100 MHz sampling rate, averaging eight samples and five consecutive plasma shots. Maximum horizontal error is ±0.01.)

The external magnetic field $\mathbf{B}_0$ is axisymmetric, with $B_{0r} \ll B_{0z}$ and $B_{0\theta}=0$. It is therefore appropriate to use a near axis expansion for the magnetic field, which means that B_{0z} is treated as a function of z only and

$$B_{0r}(r,z) = -\frac{1}{2} r \frac{\partial B_{0z}(z)}{\partial z}. \tag{24}$$

The antenna is a blade antenna shown in Fig. 2. The components of antenna current density for the $m=0$ mode are given by

$$j_{ar} = \frac{I_0}{2\pi r} H(r-R_a)[\delta(z-z_a) - \delta(z-z_a-L_a)],$$

$$j_{a\theta} = 0, \tag{25}$$

$$j_{az} = \frac{I_0}{2\pi r} H(z-z_a) H(z_a+L_a-z) \delta(r-R_a),$$

where I_0 is the amplitude of the current, L_a is the antenna length, z_a is the antenna position as shown in Fig. 2, R_a is the radius of the horizontal rod, and H is the Heaviside step function.

B. Periodic array of mirrors

It is convenient to first consider a single mirror cell ($0 \leq z \leq L_m$) with periodic boundary conditions, which provides an ideal case to study the Bragg reflection induced spectral gap as well as a benchmark for the realistic simulations of finite number of mirrors. This single mirror cell has the same sinusoidal profile of the magnetic field described in Eq. (6). The following boundary conditions are used:

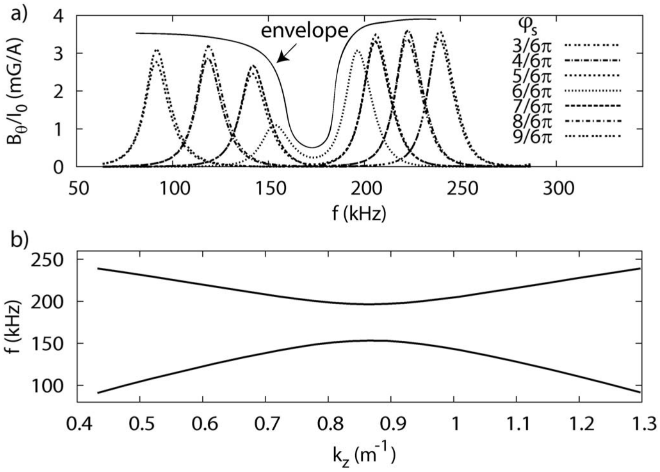

FIG. 12. (a) Simulation of wave excitation as a function of φ_s and frequency. A sharp forbidden gap of wave excitation is evident between two branches of traveling waves. Here the wave amplitude is normalized by the antenna current. (b) The dispersion relation of excited waves from the simulation, in which f corresponds to the maximum of each peak and $k_z \equiv \varphi_s/L_z$.

(1) The chamber wall at $r=0.5$ m is assumed to be a conducting boundary where the tangential components of the electric field vanish.

(2) Since all the field components are regular at $r\to 0$, there are: $B_\theta|_{r=0}=0$ and $(rE_\theta)|_{r=0}=0$ for $m=0$; $E_z|_{r=0}=0$ and $(rE_\theta)|_{r=0}=0$ for $m\neq 0$.

(3) Periodic boundary condition: $(\mathbf{E},\mathbf{B})|_{z=L_m} = (\mathbf{E},\mathbf{B})|_{z=0} e^{i\phi_s}$, where φ_s is the given phase difference between the field components at $z=0$ and $z=L_m$.

The experimentally measured radial profile of the plasma density is used in the code as shown in Fig. 3. The density is assumed to be independent of z. The collision frequency for electrons is calculated as the electron-ion Coulomb collision frequency[42] $\nu_{ei}=2.91\times10^{-12} n_e T_e^{-3/2} \ln\Lambda$, where T_e and n_e are expressed in eV and m^{-3}, respectively. The electron temperature is taken to be 8 eV; the Coulomb logarithm is taken to be $\ln\Lambda=12$. The collision frequency for ions is set to zero.

In this simulation, $L_a=0.8$ m, $z_a=1$ m, and $R_a=0.15$ m. Although the antenna launches several azimuthal modes, the amplitudes of all modes with $m\neq 0$ are significantly smaller than that of the $m=0$ mode. Therefore, only the $m=0$ mode is considered here.

The amplitude of B_θ is recorded at ($r=0.04$ m, $z=3$ m) and normalized by the antenna current I_0 with different values of the phase angle $\varphi_s \in (0, 2\pi)$ [Fig. 12(a)]. In a uniform system, the phase angle φ_s determines the value of $k_z=\varphi_s/L_z$. In the mirror configuration, the forbidden band appears around $k_m=\pi/L_z$. There are two peaks in B_θ for each value of φ_s. For various $\varphi_s \in (0,\pi)$, the lower-frequency peak represents a right-traveling wave, and the one at the higher frequency is a left-traveling wave.

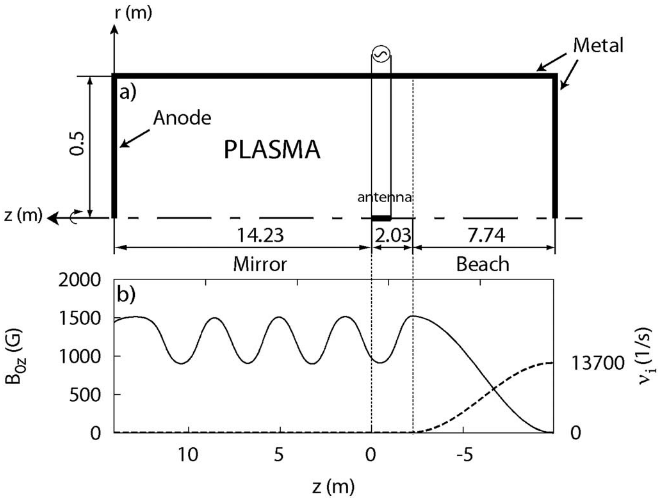

FIG. 13. Computational setup used to simulate the mirror array in the LAPD shown in Fig. 2. (a) The computational domain. (b) The z component of the external magnetic field (left) and the finite ion collision frequency in the beach area (right).

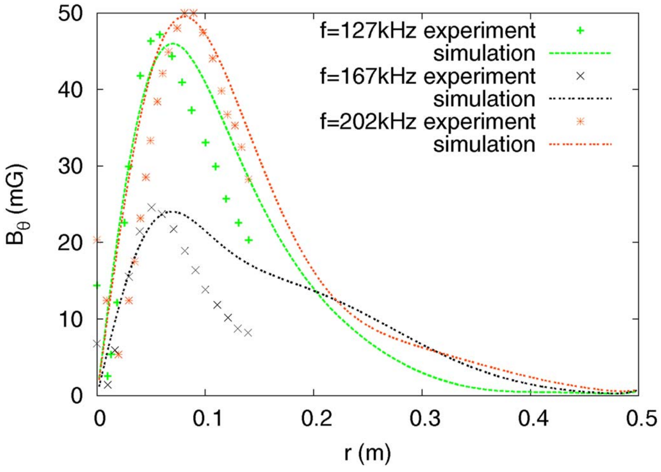

FIG. 14. (Color online) The radial profiles of azimuthal B field (rms) at three frequencies comparing simulation and experiment results. This simulation uses $\alpha=4$ which is defined in Eq. (26).

At larger values of φ_s [$\varphi_s \in (\pi, 2\pi)$], the waves in both branches change the direction of propagation, switching from the right to the left in the lower branch, and from the left to the right in the upper branch. At the transition (where $\varphi_s \approx \pi$) the wave becomes a standing wave, almost fully reflected by the mirrors due to the Bragg reflection. It is clear that a gap is formed where the wave excitation is significantly suppressed as illustrated with an envelope (solid line) in Fig. 12(a). The dispersion curves found in the simulation [Fig. 12(b)] evidently reproduced Fig. 1. More importantly, because of the definite k_z in the simulation, the gap width can be determined accurately at $k_z = k_m$, which matches the prediction of Eq. (14).

C. Mirror array system simulation for the LAPD

Now the mirror array configuration in the LAPD is considered realistically as shown in Fig. 13, with a magnetic beach as an absorbing end and the anode as a reflecting end. The magnetic beach here is longer (7.74 m) than that in the experiment to ensure complete absorption of the waves. A finite ion collision frequency ν_i is introduced to resolve the ion cyclotron resonance in the beach area. The boundary conditions in the radial direction remain the same as in the case of infinite periodic system.

To be consistent with the experiment, the z coordinate is pointing from right to left; the origin is set at the left rod of the blade antenna with $L_a = 1.0$ m, and $R_a = 0.005$ m. The variable antenna current due to rf coupling efficiency at different frequencies (Fig. 6) are used to calculate the wave field amplitude. The radial profile of B_θ for three frequencies $f = 127$ kHz, 167 kHz, and 202 kHz is shown in Fig. 14, compared with the experimental measurement at $z = 10.25$ m (port 14). The calculated quantity B_θ in the plot is $|B_\theta(f,r,z)|/\sqrt{2}$, which is equivalent to the rms average of B_θ from the measurement. The frequency scan of the radial maximum value of B_θ at $z = 3.21$ m (port 36) and $z = 10.25$ m (port 14) are compared with the experimental data in Fig. 15. Both in the simulation and the experiment, the wave signal at port 14 exhibits a gap at the same frequency as in the periodic system, while at port 36, the gap is less obvious because the detector is only one mirror away from the antenna.

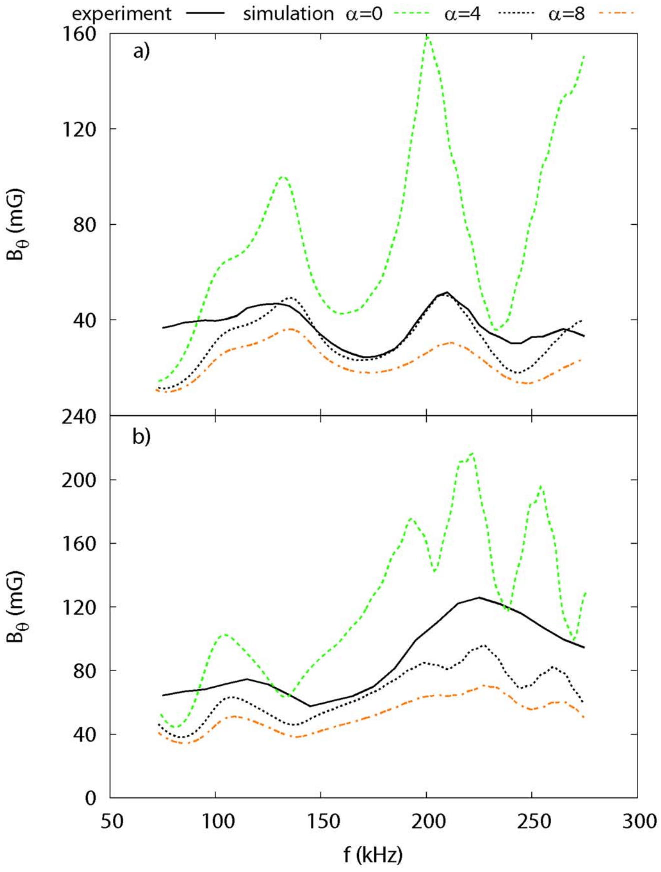

FIG. 15. (Color online) Comparison of B_θ: experiment vs the simulation at (a) port 14 and (b) port 36. The plots show the radial maximum of B_θ as a function of frequency. Three α values represent possible estimates of effective collision frequencies for Landau damping [see Eq. (26)].

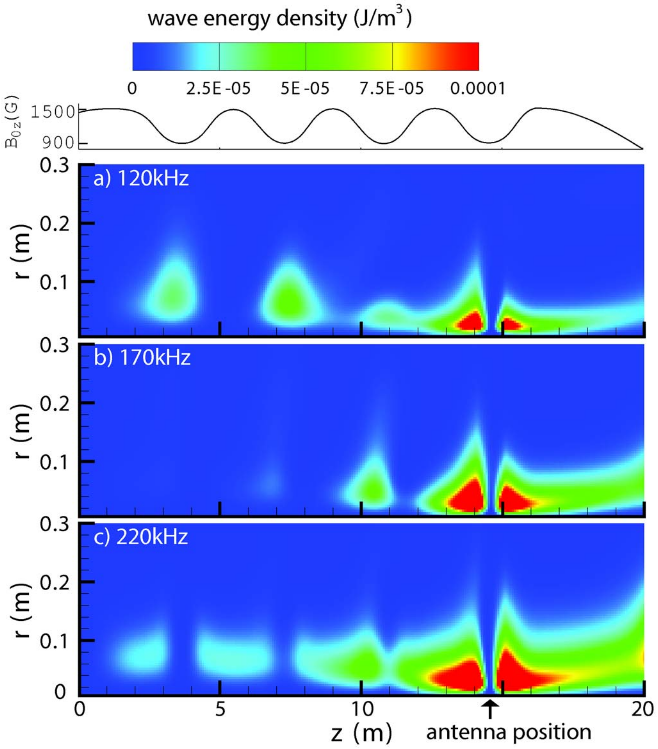

FIG. 16. (Color online) The contour plots of wave energy density obtained from Eq. (27) for three frequencies. (a) $f=120$ kHz below the gap; (b) $f=170$ kHz in the gap; (c) $f=220$ kHz above the gap.

TABLE I. Similarities between TAE and mirror array Alfvén experiment.

	Experiments	
Properties	TAE	SAW in mirror array
Periodicity	Magnetic field: $B_0\ (\theta)$	Magnetic field: $B_0\ (z)$
Periodic length	$2\pi qR$	Mirror length: L_m
B_0 modulation strength	$\hat{\varepsilon}$ (Ref. 45)	$M=\dfrac{B_{\max}-B_{\min}}{B_{\max}+B_{\min}}$
Wave function	$\sim\exp(im\theta)$	$\sim\exp(ik_{\parallel}z)$
Bragg condition	$k_{\parallel}=n/2qR$	$k_n=n\pi/L_m$
Spectral gap/ continuum	Yes	Yes
Eigenmodes	Yes	?

Additional damping mechanism beside electron-ion Coulomb collisions is needed to match the absolute value of wave amplitude. Since the electron thermal velocity is comparable to the wave phase velocity in this study, electron Landau damping can play an important role in the wave propagation. To take into account of the effect of Landau damping, an effective electron collision frequency is introduced as

$$\nu_{e\text{-Landau}}=\alpha\frac{v_{te}\omega}{v_A}, \tag{26}$$

where α is a numerical factor. As a result of the frequency dependence of $\nu_{e\text{-Landau}}$, the wave amplitude is more suppressed in the higher frequency region, which makes the shape of the scan close to that in the experiment. A good agreement of the position, depth and width of the gap at port 14 is reached in the calculation with $\alpha=4$. The agreement at port 14 is better than that at port 36, which may be due to near-field effects at port 36.

With the antenna placed in the last mirror, the waves are launched in both directions. It is instructive to characterize wave propagation by the wave energy density[43]

$$W=\frac{E_{\alpha}^{*}E_{\beta}}{4}\frac{\partial(\omega^2\varepsilon'_{\alpha\beta})}{\omega\partial\omega}, \tag{27}$$

where $\varepsilon'_{\alpha\beta}$ is the Hermitian part of the dielectric tensor neglecting the collision frequency. Figure 16 shows the 2D contour plots of the wave energy density for a frequency below the forbidden gap at $f=120$ kHz, a frequency inside the gap at $f=170$ kHz, and a frequency above the gap at $f=220$ kHz. It is seen that the wave energy is the highest at the antenna. For the frequencies away from the forbidden gap, i.e., $f=120$ kHz and 220 kHz, the wave propagates leftwards and reflects as it reaches the boundary, the anode in the experiment. The magnitude of the wave energy decreases along the propagation due to absorption. The patterns of wave energy density are similar at these two frequencies. In the forbidden gap region, e.g., $f=170$ kHz, the wave amplitude decreases faster due to the multiple reflections from the mirror cells. As a result, the wave energy diminishes as it reaches the anode. On the other hand, for all the cases, the waves propagate rightwards without much reflection until absorbed at the magnetic beach.

VI. CONCLUSIONS AND RECOMMENDATIONS FOR FUTURE WORK

In this work, the axial magnetic periodicity induced Alfvén spectral gaps and continua are discovered and characterized experimentally for the first time. The gap spectral width is found to increase with the magnetic mirror depth (M), which is predicted by solving Mathieu's equation as well as the coupled wave theory in TAE studies.[44,45] The running cross-covariance analysis shows that reflected wave from the LAPD anode/cathode enhances the features of the spectral gap. The quality factor of the spectral upper continuum is found to decrease with the plasma density.

A finite-difference simulation code successfully models this experiment in a 2D r-z plane. The results from an ideal case with periodic boundary conditions, i.e., infinite number of mirrors, show wave energy reflection near the frequency satisfying the Bragg condition. In a realistic simulation using experimental conditions at the LAPD machine, two candidate damping mechanisms, the electron-ion Coulomb collision and the electron Landau damping, are both essential in order to match the calculated spectra to the experimental ones.

To emphasize the correlation of this work with the TAE studies, the similarities between the two are summarized in Table I, where in both cases a frequency gap arises due to a periodic modulation of the ambient magnetic field. Due to the toroidal coupling in a tokamak and the magnetic shear, a certain discrete frequency can exist inside the gap, i.e., TAE modes.

In a toroidal geometry, at rational q (safety factor) magnetic surfaces, where $q=(|m|+1/2)/|n|$, two different poloidal modes m and $m+1$ couple to each other since their wave vector satisfies $k_{\parallel m}=-k_{\parallel m+1}1/R_0(n+m/q)$. Solving the two coupled eigenmode equations for poloidal electric fields,[45] the frequency difference between two continuum frequency branches is defined as the spectral gap width, $\Delta\omega=\omega_+-\omega_- \approx 2\hat{\varepsilon}|v_A k_{\parallel m}|$. From the analogy in Table I, with proper substitution of relevant quantities, the expressions for the spectral gap width in the magnetic mirror array experiment is $\Delta f_G=f_+-f_-\approx 2Mf_{\mathrm{Bragg}}$. This is shown as the blue dashed line in Fig. 9.

This work in the LAPD can provide further understanding of the TAE mode due to the benefits of simplicity and outstanding spatial and temporal resolutions. In order to create eigenmodes in this system, the axial periodicity has to be broken with a strong defect, which can be made possible by introducing a sector of magnet with much stronger background field (up to 3.5 kG) compared to the regular mirror field. The mirror field periods also need to match the reflective boundary locations at both ends in order to provide the higher Q factor for the possible modes. If the next experiment finds the eigenmodes successfully, it will be more intriguing to study fast-ion transport in these modes using the fast-ion sources[46,47] from the fast-ion group at the University of California, Irvine (UC Irvine) and an intense rf fast-ion source recently tested at the LAPD.

ACKNOWLEDGMENTS

The authors thank L. Chen and G. Y. Fu for their discussion and Z. Lucky, M. Drandell, and J. Maggs for their timely assistance at the facility and valuable contributions to this work.

This work was supported by the DOE and performed at the LAPD basic plasma user facility supported by the NSF/DOE.

[1] Lord Rayleigh, Philos. Mag. **24**, 145 (1887).
[2] C. Kittel, *Introduction to Solid State Physics*, 7th ed. (Wiley, New York, 1996).
[3] H. Kogelnik and C. V. Shank, Appl. Phys. Lett. **18**, 152 (1971).
[4] H. Kogelnik and C. V. Shank, J. Appl. Phys. **43**, 2327 (1972).
[5] C. K. Chong, D. B. McDermott, M. M. Razeghi, N. C. Luhmann, Jr., J. Pretterebner, D. Wagner, M. Thumm, M. Caplan, and B. Kulke, IEEE Trans. Plasma Sci. **20**, 393 (1992).
[6] J. J. Barroso, J. P. L. Neto, and K. G. Kostov, IEEE Trans. Plasma Sci. **31**, 752 (2003).
[7] E. Yablonovitch, T. J. Gmitter, R. D. Meade, A. M. Rappe, K. D. Brommer, and J. D. Joannopoulos, Phys. Rev. Lett. **67**, 3380 (1991).
[8] M. Bayindir, B. Temelkuran, and E. Ozbay, Phys. Rev. Lett. **84**, 2140 (2000).
[9] K. F. Casey and J. R. Matthes, J. Math. Phys. **10**, 891 (1969).
[10] C. Uberoi, Phys. Fluids **15**, 1673 (1972).
[11] D. A. D'Ippolito and J. P. Goedbloed, Plasma Phys. **22**, 1091 (1980).
[12] R. L. Dewar, R. C. Grimm, J. L. Johnson, E. A. Frieman, J. M. Greene, and P. H. Rutherford, Phys. Fluids **17**, 930 (1974).
[13] R. Betti and J. P. Freidberg, Phys. Fluids B **4**, 1465 (1992).
[14] M. S. Chu, J. M. Greene, L. L. Lao, A. D. Turnbull, and M. S. Chance, Phys. Fluids B **4**, 3713 (1992); Y. I. Kolesnichenko, V. V. Lutsenko, H. Wobig, Y. V. Yakovenko, and O. P. Fesenyuk, Phys. Plasmas **8**, 491 (2001).
[15] H. H. Duong, W. W. Heidbrink, E. J. Strait, T. W. Petrie, R. Lee, R. A. Moyer, and J. G. Watkins, Nucl. Fusion **33**, 749 (1993).
[16] R. B. White, E. Fredrickson, D. Darrow, M. Zarnstorff, R. Wilson, S. Zweben, K. Hill, Y. Chen, and G. Fu, Phys. Plasmas **2**, 2871 (1995).
[17] C. Z. Cheng, L. Chen, and M. S. Chance, Ann. Phys. **161**, 21 (1985).
[18] K.-L. Wong, Plasma Phys. Controlled Fusion **41**, R1 (1999).
[19] A. A. Ivanov, A. V. Anikeev, P. A. Bagryansky, V. N. Bocharov, P. P. Deichuli, A. N. Karpushov, V. V. Maximov, A. A. Pod'minogin, A. l. Rogozin, T. V. Salikova, and Yu. A. Tsidulko, Phys. Plasmas **1**, 1529 (1994).
[20] E. P. Kruglyakov, A. V. Burdakov, and A. A. Ivanov, AIP Conf. Proc. **812**, 3 (2006).
[21] G. Chen, A. V. Arefiev, R. D. Bengtson, B. N. Breizman, C. A. Lee, and L. L. Raja, Phys. Plasmas **13**, 123507 (2006).
[22] G. J. Morales, R. S. Loritsch, and J. E. Maggs, Phys. Plasmas **1**, 3765 (1994).
[23] G. J. Morales and J. E. Maggs, Phys. Plasmas **4**, 4118 (1997).
[24] W. Gekelman, D. Leneman, J. Maggs, and S. Vincena, Phys. Plasmas **1**, 3775 (1994).
[25] W. Gekelman, S. Vincena, D. Leneman, and J. Maggs, J. Geophys. Res. **102**, 7225, DOI: 10.1029/96JA03683 (1997).
[26] J. E. Maggs, G. J. Morales, and T. A. Carter, Phys. Plasmas **12**, 013103 (2005).
[27] M. VanZeeland, W. Gekelman, S. Vincena, and G. Dimonte, Phys. Rev. Lett. **87**, 105001 (2001).
[28] W. Gekelman, S. Vincena, and D. Leneman, Plasma Phys. Controlled Fusion **39**, A101 (1997).
[29] W. Gekelman, S. Vincena, D. Leneman, and J. Maggs, J. Geophys. Res. **102**, 7225, DOI: 10.1029/96JA03683 (1997).
[30] C. Mitchell, S. Vincena, J. Maggs, and W. Gekelman, Geophys. Res. Lett. **28**, 923, DOI: 10.1029/2000GL012165 (2001).
[31] C. C. Mitchell, J. E. Maggs, and W. Gekelman, Phys. Plasmas **9**, 2909 (2002).
[32] S. Vincena, W. Gekelman, and J. Maggs, Phys. Plasmas **8**, 3884 (2001).
[33] C. C. Mitchell, J. E. Maggs, S. T. Vincena, and W. N. Gekelman, J. Geophys. Res. **107**, 1469, DOI: 10.1029/2002JA009277 (2002).
[34] M. Abramovitz and I. A. Stegun, *Handbook of Mathematical Functions* (Dover, New York, 1972), p 722(20).
[35] H. Boehmer, M. Zales Caponi, and J. Munch, in *Free Electron Lasers*, Proceedings of the 7th Course on Physics and Technology of Free Electron Lasers of the International School of Quantum Electronics, Erice, 1980, edited by S. Martellucci and A. N. Chester (Springer, New York, 1983).
[36] D. Leneman, W. Gekelman, and J. Maggs, Rev. Sci. Instrum. **77**, 015108 (2006).
[37] S. Vincena, Ph.D. thesis, University of California, Los Angeles (1999).
[38] D. Leneman, W. Gekelman, and J. Maggs, Phys. Plasmas **7**, 3934 (2000).
[39] S. Vincena, W. Gekelman, and J. Maggs, Phys. Rev. Lett. **93**, 105003 (2004).
[40] G. Chen, A. V. Arefiev, R. D. Bengtson, B. N. Breizman, C. A. Lee, and L. L. Raja, Phys. Plasmas **13**, 123507 (2006).
[41] T. H. Stix, *Waves in Plasmas* (American Institute of Physics, New York, 1992), p. 38.
[42] P. Helander and D. J. Sigmar, *Collisional Transport in Magnetized Plasmas* (Cambridge University Press, Cambridge, UK, 2002), p. 5.
[43] V. D. Shafranov, *Reviews of Plasma Physics 3* (Consultants Bureau, New York, 1967), p. 143.
[44] G. Y. Fu and J. W. Van Dam, Phys. Fluids B **1**, 1949 (1989).
[45] H. L. Berk, J. W. Van Dam, Z. Guo, and D. M. Lindberg, Phys. Fluids B **4**, 1806 (1992).
[46] Y. Zhang, H. Boehmer, W. W. Heidbrink, R. McWilliams, D. Leneman, and S. Vincena, Rev. Sci. Instrum. **78**, 013302 (2007).
[47] H. Boehmer, D. Edrich, W. W. Heidbrink, R. McWilliams, and L. Zhao, Rev. Sci. Instrum. **75**, 1013 (2004).